Modeling Antenna Noise Temperature Due to Rain Clouds at Microwave and Millimeter-Wave Frequencies

Frank Silvio Marzano, *Senior Member, IEEE*

***Abstract*—A characterization of the antenna noise temperature due to precipitating clouds at *Ku* band and above is described by deriving a closed-form solution of the scalar radiative transfer equation. Following the so called Eddington approximation, the analytical model is based on the truncated expansion of unpolarized brightness temperature angular spectrum in terms of Legendre polynomials. The accuracy of the sky-noise Eddington model (SNEM) is evaluated by comparing it with an accurate numerical solution, taking into consideration a wide variability of medium optical parameters as well as a typical rain slab model. The effect of the antenna pattern for ground-based antennas is also quantified. Physically-based radiative cloud models, characterized by a vertically-inhomogeneous geometry, are also introduced. Hydrometeor optical parameters are calculated and modeled for a large set of beacon channel frequencies. Nimbostratus and cumulonimbus models are finally applied to SNEM for simulating slant-path attenuation and antenna noise temperatures for ground-based antennas. Results are compared with ITALSAT satellite receiver measurements and co-located radiometric data between 13.0 and 49.5 GHz for various rain events during 1998.**

***Index Terms*—Antenna noise temperature, clouds and rainfall, radio propagation, scattering, sky noise temperature.**

I. Introduction

THE growing need of larger bandwidths for communication channels has prompted a wide investigation of beacon frequencies above *Ku* band [1], [2]. At these frequencies the atmospheric effects, including both signal scintillation and fade, are not any more negligible and have to be taken into account for a correct link budget design and optimum resource allocation [3]–[7]. The impact of light-to-moderate rainfall, and even of nonprecipitating clouds, can be significant in terms not only of path attenuation, but also of sky-noise antenna temperature [8]–[10]. For marginal carrier-to-noise ratio, the system noise temperature is usually small so that the influence of sky noise temperature can substantially affect not only ground-based receiving antennas, but also transponder antennas with a multi-spot field-of-view pattern [6]. These radio propagation issues have raised a renew interest in quantifying the atmospheric attenuation and sky noise temperature at microwave and millimeter-wave bands. Whereas clear-air effects are fairly well understood and predicted, at *Ku* band and above the impact due to clouds and precipitation is generally treated from an empirical point of view [11]–[13]. International recommendations on radio propagation suggest methods which are mostly based on conventional measurements below 20 GHz, whereas prediction models are generally tested only up to 30 GHz [13]. Their validity is generally based on a statistical tuning on relatively long-term scales, whereas underlying electromagnetic (EM) models are strongly simplified as in the case of rain uniform slabs with single-scattering assumption. Indeed, multiple scattering incoherent effects can become appreciable when a millimeter-wave link is through rainfall [14], [15].

In order to accomplish an accurate characterization of these microwave and millimeter-wave channels, one could resort to experimental links which are, however, not always easy and cost-effective to set up [16], [17]. As an alternate choice, physical radiative models can be developed with the advantage to deal with a versatile and powerful methodology, but, on the other hand, with the need to describe in a fairly complete way the predominant EM processes of atmospheric wave propagation (e.g., [18]–[20]). The modeling of measured sky noise temperature due to clouds and precipitation requires an appropriate theoretical framework [8], [21]. A way to rigorously approach electromagnetic propagation in a scattering medium is to resort to the radiative transfer equation (RTE) (e.g., [21], [22]). Crude approximations of RTE, like those interpreting the medium effective temperature as its physical temperature, should be avoided because quite inaccurate to describe rain clouds in various intensity regimes [13], [23]. Complete numerical solution of RTE may be computationally intensive especially when embedded in iterative procedures [24], [15]. The uncertainty within the description of atmospheric model inputs (e.g., cloud structure, hydrometeor distribution, meteorological state) can contribute as a potentially large source of error and further reduces the intrinsic value of RTE precise mathematical models for many applications [25], [26]. Finally, in radio propagation it is also customary to avoid too complex numerical models and try to deal with relatively simple and effective approximations of the phenomenon having in mind link budget design tradeoffs [27].

In view of these open issues, the aims of this work are: i) to illustrate an accurate analytical model of sky noise temperature due to rain clouds where all main scattering parameters can be explicitly modeled through regressive formulas; ii) to apply this analytical model to physically-based synthetic rain clouds in order to evaluate the sensitivity of modeled sky noise temperature to atmospheric vertical inhomogeneity at *Ku* band

Manuscript received August 18, 2005; revised November 20, 2005. This work was supported in part by the Italian Ministry of University and Research (MIUR) and in part by the Italian Space Agency (ASI).

The author is with the Department of Electronic Engineering, University "La Sapienza" of Rome, Italy and also with the Center of Excellence CETEMPS, University of L'Aquila, Italy (e-mail: marzano@die.uniromal.it).

Digital Object Identifier 10.1109/TAP.2005.872571

and above; iii) to validate this analytical model both numerically using well-documented and accurate algorithms and experimentally using a large set of Earth-satellite measurements at *Ka*, *K*, and *V* band.

Consistently with the aforementioned objectives, the paper is organized as follows. In Section II, after a brief introduction of the theoretical framework and basic terminology, a closed-form solution of the radiative transfer equation is derived adopting the so called Eddington approximation and extending it by means of a scaling technique in Appendix A. These results, focused on ground-based antennas, are numerically validated and also extended to satellite-based antenna observations in Appendix B. In Section III the sky-noise Eddington model (SNEM) is applied to synthetic rain-cloud vertical structures, providing regressive models of rain cloud optical parameters and a quantification of the impact of ice hydrometeors. The sky-noise temperature simulations of nimbostratus and cumulonimbus rain-clouds are compared and validated against ITALSAT satellite receiver data at *Ka* band and above. Section IV is finally dedicated to a summary and a discussion of potentials and limitations of the proposed model.

II. Modeling Sky Noise Temperatire

Antenna noise temperature T_A can be computed as a convolution between the directivity gain D of the antenna and the incident brightness temperature T_B due to the atmospheric and environmental scenario [27]. Sky-noise T_B can vary from few kelvins up to hundreds of kelvins depending on the frequency and the presence of gases, clouds and rainfall along the path. An atmosphere with clouds and rain can be modeled as an absorbing and scattering medium characterized by a polydispersion of hydrometeors having different size, composition and shape [28], [29]. At a given frequency ν and for unpolarized radiation, the volumetric extinction coefficient is defined by $k_{\rm e} = k_{\rm a} + k_{\rm s}$, being $k_{\rm a}$ the volumetric absorption coefficient and $k_{\rm s}$ the volumetric scattering coefficient. If EM scattering is symmetric about the incident wave direction, the volumetric scattering phase function p can be introduced by

$$p(\mu_s) = 4\pi \frac{k_d(\mu_s)}{k_s} = 4\pi \frac{k_d(\mu_s)}{\int_0^{2\pi}\int_{-1}^{1} k_d(\mu,\varphi,\mu',\varphi')d\mu' d\varphi'} \quad (1)$$

where k_d is the volumetric differential scattering coefficient and $\mu_{\rm s} = \cos\Theta_s$ is the cosine of the scattering angle Θ_s. The latter is the angle between the incident (θ',φ') and scattering (θ,φ) EM wave directions, expressed by

$$\mu_s = \cos(\Theta_s) = \mu\mu' + \sqrt{(1-\mu^2)(1-\mu'^2)}\cos(\varphi-\varphi') \quad (2)$$

where the cosine of polar angle θ is indicated by $\mu = \cos\theta$. The normalization of p in (1) is assumed to be to 4π—note that this normalization of p may be different from others also used in literature [28]. The volumetric albedo w is defined as $w = k_{\rm s}/k_e$, which is a measure of scattering efficiency (e.g., a nonscattering atmosphere has a null albedo). The atmospheric optical parameters k_e, w, and p can be computed once known the properties of the hydrometeor polydispersion. The EM radiation, impinging on the receiving antenna, will be the result of the extinction, emission and multiple scattering processes in the atmosphere with clouds and rainfall. A theoretical framework to model the received T_B is given by the radiative transfer theory [28], [29].

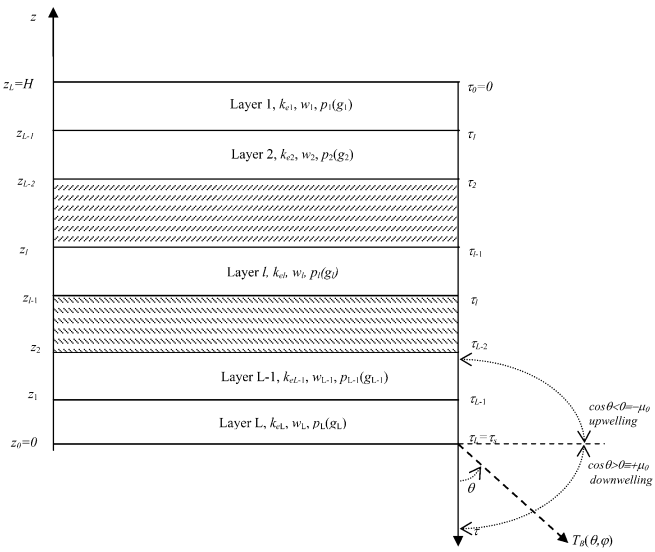

Fig. 1. Schematic illustration of a stratified medium along the vertical coordinate z, having a thickness H and composed of L adjacent layers characterized by three optical parameters: extinction coefficient k_e, albedo w and phase function p (or asymmetry factor g). The layer are numbered from the medium top in an increasing order $(l = 1, 2, \ldots, L)$. The optical thickness coordinate τ is opposite to z with its origin $\tau = \tau_0 = 0$ corresponding to $z = z_L = H$. The medium bottom surface is at $\tau_L = \tau_s = 0$ corresponding to $z = 0$. Downwelling and upwelling angles of antenna noise temperature $T_A(\theta,\varphi)$ are also indicated, emphasizing the adopted convention for $\cos(\theta)$.

A. Radiative Transfer Framework

Let us consider a horizontally-stratified atmosphere with a bottom level at $z = 0$ (surface) and a top height at $z = H$, as in Fig. 1. A plane-parallel geometry is generally an appropriate assumption because gravity forces a density stratification. Fig. 1 schematically depicts the medium geometry in the general case of L layers and the relative coordinate system, which will be used throughout this paper. A vertical coordinate (along z) in terms of vertical optical thickness τ or path attenuation A [dB] at frequency ν can be defined as

$$\tau(z) = \frac{10}{\ln(10)}A(z) = \int_z^H k_e(z')dz' = \int_z^H [k_s(z') + k_a(z')]dz' \quad (3)$$

where $\tau = 0$ at $z = H$ and $\tau = \tau_{\rm s}$ at $z = 0$ with k_e explicitly dependent on z, as in Fig. 1. The polar angle θ is defined for $0 \le \theta \le \pi$ such that $0 \le \theta \le /2$ and $\pi/2 \le \theta \le \pi$ hold for downward directions and upward directions, respectively. For simplicity of notation, we have dropped the frequency dependence of optical parameters.

For a plane-parallel stratified atmosphere, the unpolarized brightness temperature $T_B(\tau,\mu,\varphi)$, observed at τ for a frequency ν along μ and φ, satisfies the integro-differential *radiative transfer equation* (RTE). Notice that this is equivalent to describe the behavior of the first parameter of the Stokes polarization vector [28]. The azimuthal dependence of T_B can be due to: i) anisotropic sources of emitted radiation and

multiple scattering; ii) horizontally finite dimension of the atmosphere; and iii) azimuthal asymmetry of surface reflectivity. If we can exclude all these causes, the dependence of T_B on φ may be omitted. In other words, if we integrate $T_B(\tau,\mu,\varphi)$ with respect to φ over 2π and define an azimuthally-average brightness temperature $T_B(\tau,\mu)$ and an azimuthally-averaged scattering phase function p_a, consistently with Fig. 1 the RTE can be written as

$$\mu\frac{dT_B(\tau,\mu)}{d\tau} = -T_B(\tau,\mu) + J(\tau,\mu) \tag{4}$$

where the pseudo-source function J is expressed by

$$J(\tau,\mu) = \frac{w(\tau)}{2}\int_{-1}^{+1} p_a(\tau,\mu,\mu')T_B(\tau,\mu')d\mu' + [1-w(\tau)]T(\tau) \tag{5}$$

with T the physical temperature and where the medium parameters have been assumed dependent on τ. The first term of J is sometimes referred to as the multiple scattering source, while the second term represents thermal emission. It is worth mentioning that the same equation for $T_B(\tau,\mu)$ can be obtained by expanding the brightness temperature in a Fourier cosine series with respect φ and then taking the zero-order term.

It is convenient to introduce the polar-angle cosine modulus $\mu_0 = |\cos\theta|$ with $0 \le \mu_0 \le 1$ so that $T_B(\tau,\mu_0)$ and $T_B(\tau,-\mu_0)$ hold for downwelling and upwelling brightness temperatures, respectively (and the same applies to all functional dependence on μ_0). Then, referring to Fig. 1, $T_B(\tau_{\rm s},\mu_0)$ at $\tau=\tau_{\rm s}$ can be formally expressed by means of RTE integral form

$$T_B(\tau_s,\mu_0) = T_B(0,\mu_0)e^{-\tau_s/\mu_0} + \frac{1}{\mu_0}\int_0^{\tau_s} J(\tau,\mu_0)e^{-(\tau_s-\tau)/\mu_0}d\tau. \tag{6}$$

The above expression is only a formal solution since the source function J is actually depending on T_B itself. The solution of (4) can be derived once the boundary conditions are imposed. This physically means that, in case of a scattering medium, surface EM diffusion is coupled with atmospheric radiation. For a rough surface, such as an idealized land, a Lambertian surface emissivity model $e_{\rm sL}$ can be adopted if the surface differential reflectivity can be assumed independent of angle. At the top of the atmosphere at $\tau=0$ and for a Lambertian random surface at $\tau=\tau_{\rm s}$, it holds

$$\begin{cases} T_B(0,\mu_0) = T_c \\ T_B(\tau_s,-\mu_0) = e_{\rm sL}T_s + (1-e_{\rm sL})2\pi\int_0^1 T_B(\tau_s,\mu_0')\mu_0'd\mu_0' \end{cases} \tag{7}$$

where $T_c = 2.73$ K is the cosmic background brightness temperature at microwave and $T_{\rm s}$ is the surface temperature. For a specular surface, such as a calm sea, the differential reflectivity can be expressed through the polarization-dependent Fresnel reflection coefficients (see Appendix B).

B. Sky-Noise Eddington Model for Uniform Atmosphere

Let us consider, for simplicity, a uniform atmospheric layer between $\tau=0$ and $\tau=\tau_s$ of thickness H. In this circumstance RTE exhibits constant coefficients, that is the optical parameters p_a, w, and k_e become independent of (optical) distance. A way to approach the solution of RTE is to expand the angular spectrum of the phase function p_a in terms of Legendre polynomials P_n of order n, satisfying the orthogonality property in the $(-1,1)$ interval. Under the hypothesis of symmetric scattering, we can write [28]

$$p_a(\mu,\mu') = \sum_{n=0}^{N}(2n+1)h_nP_n(\mu)P_n(\mu') \tag{8}$$

where h_n are the Legendre polynomial expansion coefficients with $P_0(\mu)=1, P_1(\mu)=\mu$ and recursively for nth-order polynomials. In many applications the truncation of this Legendre series to the first order (i.e., $N=1$), also called *Eddington's approximation* [40], is quite effective [30], [31]. The average scattering phase function then becomes

$$p_a(\mu,\mu') \cong h_0 + 3h_1\mu\mu' = 1 + 3g\mu\mu' \tag{9}$$

being the weights h_o and h_1 given by $h_0=1$ and $h_1=g$ with g, by definition, the asymmetry factor of the scattering phase function p_a [15]. It is worth mentioning that (9) coincides with the Sobolev approximation of p_a [32] and that it can be also obtained as azimuth average of $p(\mu_{\rm s}) = 1+3g\mu_{\rm s}$. The physical constraint $p_a \ge 0$ implies that $g \ge (-1/3)$ in (9). Analogously to p_a, the angular spectrum of T_B can be also expanded in terms of Legendre polynomials P_n and truncated at $N=1$

$$T_B(\tau,\mu) = \sum_{n=0}^{N} T_{Bn}(\tau)P_n(\mu) \cong T_{B0}(\tau) + \mu T_{B1}(\tau) \tag{10}$$

where the expansion coefficients have been grouped in the terms $T_{\rm Bn}(\tau)$ [40]. The knowledge of $T_{B0}(\tau)$ and $T_{B1}(\tau)$ completely solves the RTE under Eddington's approximation.

The detailed derivation of the approximate solution of (6) coupled with (7), using (9) and (10), is given in Appendix A. The proposed technique solves for $T_{B0}(\tau)$ and $T_{B1}(\tau)$, evaluates the source function $J_{\rm E}(\tau,\mu)$ from (5) and then expresses the closed-form solution via (6). For ground-based antennas and a uniform atmosphere, the closed form of the sky-noise Eddington model (SNEM) then reduces to

$$\begin{aligned} T_B(\tau_s,\mu_0) = {} & T_ce^{-\tau_s/\mu_0} + \left[t_0 - t_1\mu_0 - \frac{wg\mu_0}{(1-wg)}t_1\right] \\ & \times (1-e^{-\tau_s/\mu_0}) + t_1\tau_s \\ & - wC_1\frac{1+c\mu_0 g}{1-\lambda\mu_0}(e^{-\tau_s/\mu_0} - e^{-\lambda\tau_s}) \\ & - wC_2\frac{1-c\mu_0 g}{1+\lambda\mu_0}(e^{-\tau_s/\mu_0} - e^{\lambda\tau_s}) \end{aligned} \tag{11}$$

where the optical parameters τ_s, w, and g are transformed by *delta-Eddington* similarity equations, given in Appendix A. As a simple test, for a homogeneous slab with no scattering having $w=0$ (i.e., $k_s=0$), and uniform temperature $T_0=t_0$ (and $t_1=0$), previous equation reduces to

$$T_B(\tau_s,\mu_0) = T_ce^{-\tau_s/\mu_0} + T_0(1-e^{-\tau_s/\mu_0}) \tag{12}$$

which is the well-known RTE solution for ground-based radiometric observations of absorbing media. If τ_s includes also scattering contributions (i.e., $\tau_s = k_a H + k_s H$), (12) also expresses the simplified formula suggested to compute sky noise temperature due to rain clouds with $T_0 = 275$ K [13]. Note that Appendix B is devoted to the extension of (11) to satellite-based antennas.

C. Numerical Validation

The validation of the analytical radiative transfer model, described above, can be performed by resorting to RTE numerical solutions, well tested and documented in literature. Among the various RTE codes available, the discrete ordinate unpolarized radiative transfer (DisORT) is one of the most accurate and widely used for inter-comparison purposes [24]. Within DisORT the atmosphere is assumed to consist of L adjacent homogeneous layers in which w, k_e, and p_a are taken to be constant within each layer. Physical temperature is supposed to be linearly dependent on the vertical coordinate within each layer. The angular variation in μ is discretized into $2N_\mu$ directions so that the multiple scattering is transformed into a sum by means of a Gaussian quadrature (which implicitly ensures the normalization of the phase function).

Our tests are devoted to the validation of radiance (brightness temperature) results and not to their angular integral in terms of flux density, defined in (A.9), and described in [33]. We will let the optical parameters to vary independently within the whole range of their definition domain. This test is an extreme one, but it stresses the mathematical conditions where the solution denotes its limitations even though these limits may be not of physical importance. In order to reduce the numerical burden of computation, we have sampled the variation of the key radiative parameters. In particular, we have selected τ between 0.1 and 50, w between 0.1 and 0.9, g between 0 and 0.9, and the polar angle θ between 0° and 75°. A linearly decreasing temperature has been assumed with a surface temperature of 293.0 K and a top temperature of 273.0 K. The surface has been supposed Lambertian with an emissivity of 0.9. In case of DisORT computations, a Heyney-Greenstein phase function has been assumed with the number of streams $N_\mu = 16$ [34].

Fig. 2 shows the histogram of percentage brightness temperature error, defined as 100 $(T_B - T_{B\mathrm{DISORT}})/T_{B\mathrm{DISORT}}$, for ground-based antennas at zenith when avoiding and when using the delta-Eddington transformation of optical parameters (see Appendix A). When the delta-Eddington transformation is not applied, an average error of about 25% is obtained with peaks more than 50% in some critical circumstances. The errors are generally larger for smaller optical thickness (i.e., smaller extinction), higher albedo and asymmetry factor and smaller zenith angles. A major source of discrepancy may be attributed to the behavior of the scattering phase function which, in case of a Sobolev approximation, is significantly different from that of Heyney–Greenstein [35]. When using the delta-Eddington transformation, it is apparent that in all cases the overall percentage error is drastically reduced to less than 5%, still with the same trend with respect to the optical parameters. Indeed, very low optical thickness values are rarely associated to large volumetric albedo and scattering asymmetry for natural media.

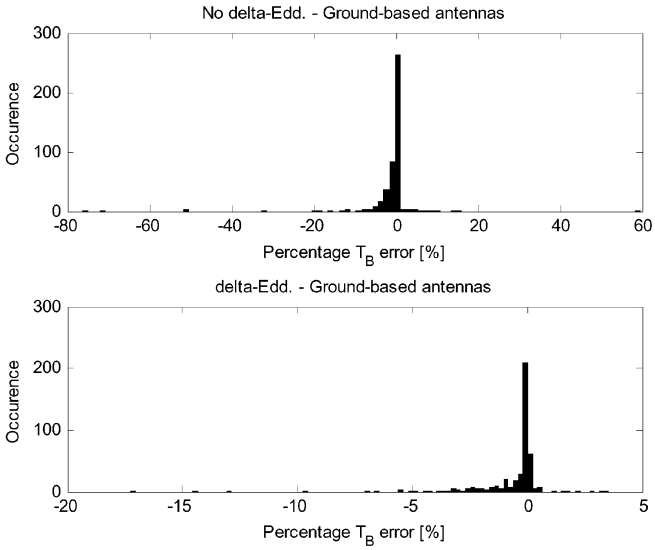

Fig. 2. Occurrence of percentage brightness temperature error, defined as $100(T_B - T_{B\mathrm{DISORT}})/T_{B\mathrm{DISORT}}$, for ground-based antennas at zenith when avoiding (top panel) and when using (bottom panel) delta-Eddington transformation of optical parameters. Simulations refer to a homogeneous layer of variable optical thickness τ, albedo w and asymmetry factor g with a Lambertian surface temperature of 293 K and a top temperature of 273 K.

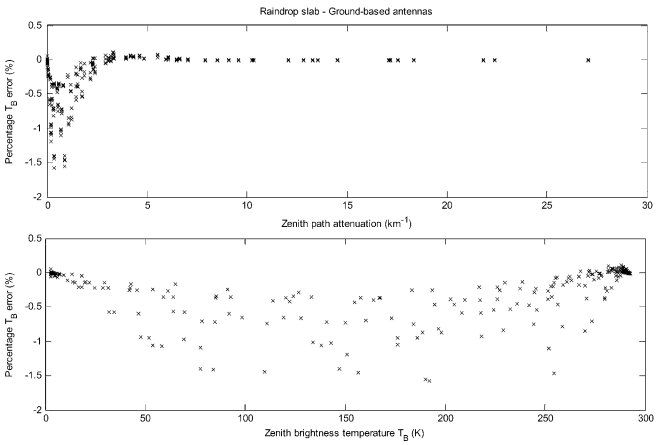

Fig. 3. Percentage brightness temperature error, defined as in Fig. 2, as a function of the vertical path attenuation A and brightness temperature T_B for ground-based antennas at zenith. Results refer to a slab of spherical raindrops of thickness 3 km with surface temperature of 293.0 K and a top temperature of 273.0 K above a Lambertian surface. Frequency range goes from 10 to 90 GHz and observation angles from 0 to 80°, whereas rain-rates are between 0 and 100 mm/h.

Thus, the tails of the percentages errors larger than 5% are due to the fact that we have arbitrarily neglected the mutual relationship among the optical parameters.

As a more realistic model of a scattering medium, we have chosen a uniform rain slab of 3 km with surface temperature of 293.0 K and a top temperature of 273.0 K, above a Lambertian surface with an emissivity of 0.9. A Marshall-Palmer drop size distribution [41] has been used to compute the optical parameters under the assumption of spherical liquid particles (see Section III). The delta-Eddington transformation has been adopted for T_B calculations. Frequency range goes from 10 to 90 GHz and observation angles from 0 to 75°, whereas rain-rates are set between 0.01 and 100 mm/h. Fig. 3, shows the percentage T_B

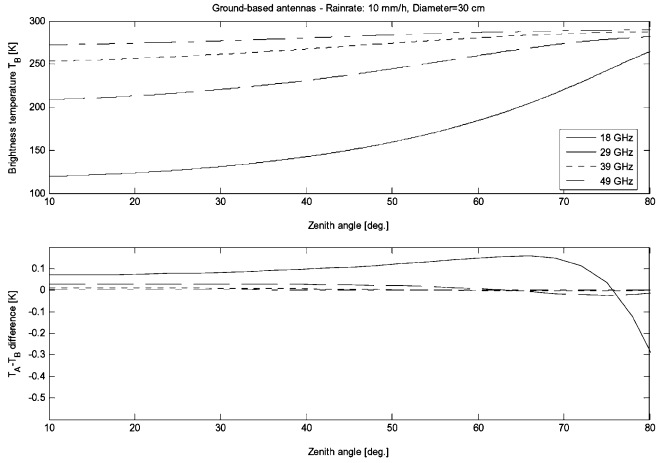

Fig. 4. Effects of the antenna pattern for ground-based antennas on the observation of a 3-km rain slab with a 10 mm/h and 10 mm/h precipitation rate. Top panel shows the angular spectrum of the incident brightness temperature T_B, whereas in the bottom panel sky noise temperature (T_A) and brightness temperature difference is shown for a parabolic antenna with a diameter of 30 cm.

error, defined as in Fig. 2, as a function of the vertical path attenuation A and sky noise temperature T_B for ground-based antennas. Using the rain slab model, the overall percentage errors are less than 2% with a tendency to underestimate the true T_B value. The larger underestimation is for smaller values of optical thickness. This may be explained taking into account that, since albedo weights the multiple scattering effects [see (5)] mostly governing the T_B angular spectrum, in this region of τ the errors due to the first-order approximation of T_B zenith variations are not compensated by extinction effects.

D. Antenna Pattern Effects

We have shown the previous results in terms of observed brightness temperature T_B. It is interesting to evaluate the effect of the antenna pattern when observing a rain medium in order to quantify the differences with respect to the received antenna noise temperature T_A. The latter is given by [27]

$$T_A(\tau_s) = \frac{1}{4\pi}\int_0^{2\pi}\int_{-1}^{1} D(\mu,\varphi)T_B(\tau_s,\mu,\varphi)d\mu d\varphi \qquad (13)$$

where D is the antenna directive gain. For simplicity, let us assume a Gaussian-shape for the antenna pattern with $\theta_{\rm HP}$ the half-power antenna beam-width. The latter, for a parabolic antenna of diameter D_a, can be approximated by $\theta_{\rm HP} \cong 29\lambda/D_a$ with λ the wavelength (e.g., [15]). Thus, the downwelling antenna noise temperature can be expressed by

$$T_A(\tau_s) = \frac{4\ln 2}{\theta_{\rm HP}^2}\int_0^1 T_B(\tau_s,\mu_0)e^{-(\ln 2)\left(\frac{\cos^{-1}\mu_0}{\theta_{\rm HP}}\right)^2}d\mu_0. \qquad (14)$$

In order to test the difference $T_A - T_B$, using (14), we have selected the rain slab model of 3 km and a variable rain-rate, considering an antenna with a diameter of 30 and 120 cm to set up its field-of-view.

As an example, Fig. 4, shows the effects of the antenna pattern for a ground-based antenna of 30-cm diameter on the observation of a 3-km rain slab with a 10 mm/h precipitation rate. The results are plotted in terms of the off-zenith angular spectrum of incident T_B and of $T_A - T_B$ difference. The behavior of T_B as a function of zenith angle is expected: as zenith angle tends to 90° (horizon), T_B tends to saturate since the rain slab is horizontally stratified and its path attenuation becomes larger and larger. The angular behavior of T_B is quite smooth and this explains the very small effects of antenna pattern integration. As expected, this $T_A - T_B$ difference is larger for smaller antennas and lower frequencies since the corresponding antenna beam-width becomes larger. As the rain-rate increases, the noise temperature difference further decreases as the angular behavior of T_B is much smoother. These plots support the choice to deal with T_B instead of T_A for ground-based antennas being their difference less than 0.2 K.

III. Characterizing Sky Noise Temperature

The delta-Eddington analytical solution, described in the previous section, has been derived, for simplicity, considering a homogeneous atmospheric layer. Realistic structures of clouds and precipitation generally show a strong vertically inhomogeneity. The finite horizontal extent of clouds cannot be considered in a rigorous manner within our sky-noise Eddington model. However, on one hand, highly directive ground-based antennas, used in microwave and millimeter-wave applications, partially minimize the problem of nonuniform beam filling. On the other hand, parametric approaches (such as weighing raining cloud and clear-air areas by means of semi-empirical factors or equivalent 1-D slant geometries) can still be applied to obtain an approximate analytical solution to the radiative transfer problem [22], [23].

A. Sky Noise Temperature Due to Inhomogeneous Rain Clouds

The vertically inhomogeneous atmosphere, modeling a rain cloud, is divided into L layers as in Fig. 1. The associated $L+1$ vertical levels are indicated by optical depths $\tau_0, \tau_1, \ldots, \tau_{L-1}, \tau_L$, where the layer number and optical depth increase from the top to bottom of the atmosphere, that is $\tau{=}\tau_0 = 0$ for $z = H$ and $\tau{=}\tau_L{=}\tau_{\rm s}$ for $z = 0$. The basic assumption is that each layer is homogeneous so that *delta-Eddington* transformed optical parameters $k_{\rm el}, w_l$, and g_l of lth layer are constant. In accordance with previous parameterizations, the temperature T_l within each layer is assumed linearly dependent on τ

$$T_l(\tau) = t_{0l} + t_{1l}(\tau - \tau_{l-1}) = T(\tau_{l-1}) + \frac{\Gamma_{Tl}}{k_{el}}\tau_l \qquad (15)$$

where $\tau_{l-1} < \tau < \tau_l$ and the (positive) thermal lapse rate Γ_{Tl} may be different from layer to layer. The thermal structure of the stratified atmosphere is thus determined by $2L$ constants. Exploiting the results already obtained for a single layer, under the Eddington approximation, the analytical solution of RTE is for the lth layer ($l = 0, 1, 2, \ldots, L$) with $\tau_{l-1} < \tau < \tau_l$ is

$$\begin{cases} T_{B0}^{(l)}(\tau) = C_{1l}e^{-\lambda_l\tau} + C_{2l}e^{\lambda_l\tau} + t_{0l} + t_{1l}\tau \\ T_{B1}^{(l)}(\tau) = c_l C_{1l}e^{-\lambda_l\tau} - c_l C_{2l}e^{\lambda_l\tau} - \frac{t_{1l}}{1-w_l g_l} \end{cases} \qquad (16)$$

where c_l and λ_l are the terms c and λ specific for the lth layer

$$\lambda_l = \sqrt{3(1-w_l g_l)(1-w_l)}, \quad c_l = \sqrt{\frac{3(1-w_l)}{1-w_l g_l}}. \tag{17}$$

The $2L$ integration constants C_{1l} and $C_{2l}(l = 1,2,\ldots,L)$ are relative to lth layer and can be determined by imposing not only the boundary conditions at $\tau = 0$ and $\tau = \tau_L = \tau_s$, but also the continuity equations at the $L-1$ intermediate boundaries, i.e., at $\tau_{=}\tau_l$ with $l = 1,\ldots,L-1$. Generalizing (7), in terms of flux densities (see Appendix A) we have (18), shown at the bottom of the page, with $l = 1,\ldots,L-1$ and $T_B^{(l)}$ is the T_B belonging the lth layer. After substituting (16) into (18), the linear system in (18) represents a set of $2L$ equations in $2L$ unknowns which are the integration constants C_{1l} and $C_{2l}(l = 1,2,\ldots,L)$. A numerical solution of the previous linear system provides all $2L$ integration constants and, therefore, the complete expression of $T_{B0}(\tau)$ and $T_{B1}(\tau)$ in (16) for each atmospheric layer. A scaling transformation is appropriate in order to avoid unwanted singularities during the inversion procedure [36]. From Appendix A, we know that the integration constants C_{1l} and C_{2l} can be transformed as

$$\begin{cases} C_{1l} = \tilde{C}_{1l} e^{\lambda \tau_{l-1}} \\ C_{2l} = \tilde{C}_{2l} e^{-\lambda \tau_l}. \end{cases} \tag{19}$$

Previous expressions can be applied to ground-based observations in a straightforward manner using a recursive approach. The set of recursive equations to determine the SNEM downwelling $T_B(\tau_l, \mu_0)$ at the lth atmospheric level τ_l is

$$\begin{aligned} &T_B(\tau_0{=}0, \mu_0) = T_c \\ &T_B(\tau_l, \mu_0){=}T_B(\tau_{l-1}, \mu_0) e^{-(\tau_l - \tau_{l-1})/\mu_0} \\ &\quad + \left[t_{0l} - t_{1l}\mu_0 - \frac{w_l g_l \mu_0}{(1-w_l g_l)} t_{1l} \right] (1 - e^{-(\tau_l - \tau_{l-1})/\mu_0}) \\ &\quad + t_{1l} \left[\tau_l - \tau_{l-1} e^{-(\tau_l - \tau_{l-1})/\mu_0} \right] \\ &\quad - w_l C_{1l} \frac{1 + c_l \mu_0 g_l}{1 - \lambda_l \mu_0} e^{-\lambda \tau_{l-1}} \left[e^{-(\tau_l - \tau_{l-1})/\mu_0} - e^{-\lambda_l (\tau_l - \tau_{l-1})} \right] \\ &\quad - w_l C_{2l} \frac{1 - c_l \mu_0 g_l}{1 + \lambda_l \mu_0} e^{\lambda \tau_{l-1}} \left[e^{-(\tau_l - \tau_{l-1})/\mu_0} - e^{\lambda_l (\tau_l - \tau_{l-1})} \right] \end{aligned} \tag{20}$$

with $l = 1,\ldots,L$ and where all terms have been already defined.

B. Radiative Models of Inhomogeneous Rain Clouds

One of the main problems to simulate clouds and precipitation is to model their spatial variability [37]. Simple *ad hoc* models, such as uniform slabs, can be useful to appraise the main radio propagation features, but can be misleading when trying to interpret and quantify real beacon and sky noise measurements [10], [14]. A way to approach to this problem is to resort to the use of mesoscale cloud-resolving three-dimensional (3-D) dynamical models which can provide output grids at a given time within a simulation of a selected meteorological event (e.g., [15], [38], [39]). The inherent advantage of this technique is to deal with physically-consistent cloud distribution in space due to the explicit microphysics describing the cloud formation and evolution.

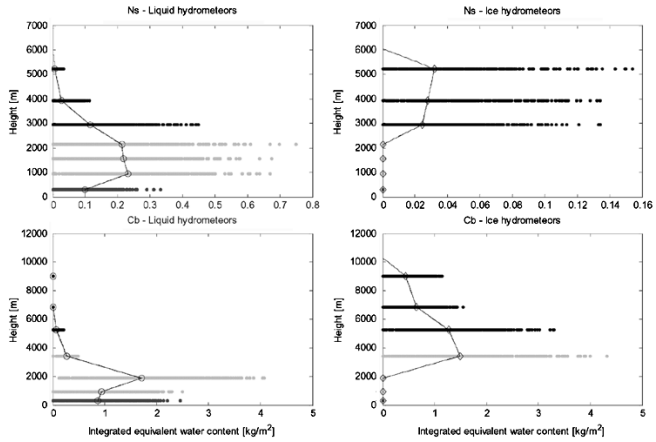

Fig. 5. Vertical profiles of liquid (left panels) and ice (right panels) hydrometors for clouds classified as Nimbostratus (Ns) and Cumulonimbus (Cb). Profiles are expressed in terms of the integrated equivalent water content within each layer (so that the vertical sum provides the total columnar content). The symbols refer to the average value within each layer, while the point dispersion around them gives an example of all possible realizations within the generated ensemble. A middle-season meteorological condition ($T_s = 22°C$) is supposed for the embedded clear-air state.

In this work numerical outputs of a 3-D time-dependent cloud mesoscale model of continental storms have been used for generating cloud-structure data set, explicitly describing the gross vertical distribution of five species of hydrometeors: cloud droplets, raindrops, graupel particles, ice crystals and snow particles. The physical-statistical methodology to randomly generate rain-cloud profiles is widely illustrated in previous works [38], [39] and only the results will be commented here. We have considered both stratiform and convective clouds, vertically described by seven homogeneous layers ($L = 7$ in (18)). For a given meteorological scenario, a data set of 5000 rain-cloud vertical structures has been statistically generated, retaining the physical and statistical features of the input microphysical cloud model through its hydrometeor content correlation matrices [38], [39]. As an example, Fig. 5 shows vertical profiles of liquid and ice hydrometeors for clouds classified as Nimbostratus (Ns) and Cumulonimbus (Cb), respectively. Profiles are expressed in terms of the integrated equivalent water content within each layer so that their sum provides the total columnar content. The profiles of Fig. 5,

$$\begin{cases} T_{B0}^{(1)}(\tau_0) + \frac{2}{3} T_{B1}^{(1)}(\tau_0) = T_c \\ T_{B0}^{(l)}(\tau_l) = T_{B0}^{(l+1)}(\tau_l) \\ T_{B1}^{(l)}(\tau_l) = T_{B1}^{(l+1)}(\tau_l) \\ T_{B0}^{(L)}(\tau_L) - \frac{2}{3} T_{B1}^{(L)}(\tau_L) = e_s T_S + (1 - e_{sL}) \left[T_{B0}^{(L)}(\tau_L) + \frac{2}{3} T_{B1}^{(L)}(\tau_L) \right] \end{cases} \tag{18}$$

refer to a middle-season mid-latitude meteorological condition, characterized by a surface temperature, relative humidity and pressure equal to 22°C, 90% and 1010 hPa, respectively, and a temperature vertical gradient, humidity height scale and pressure height scale equal to 6.5°Ckm^{-1}, 1.3 km^{-1} and 7 km^{-1}, respectively. The vertical extension of Ns and Cb synthetic clouds can be up to 6 km and 10 km, respectively, with a significant difference of hydrometeor content values. Abundant ice content above the freezing level (around 3 km) is typical of convective profiles, whereas liquid water above 3 km may indicate the presence of super-cooled droplets [37].

The hydrometeor size spectra have been characterized, except for cloud droplets, by an inverse-exponential particle size distribution (PSD)

$$N_h(r) = N_0 e^{-\Lambda r} \tag{21}$$

where the subscript "h" stands for the hth hydrometeor, r is the radius, N_0 [m^{-3} mm^{-1}] is the intercept in the logarithmic plane (proportional to the particle concentration) and Λ is the slope. Equation (21) resembles the well-known Marshall-Palmer PSD [41], but only one parameter (the slope Λ) is parameterized to the precipitation rate R [mm/h] being the intercept N_0 determined by the hydrometeor equivalent liquid water content L_h through

$$N_0 = \frac{L_h}{[\gamma(4, \Lambda r_M) - \gamma(4, \Lambda r_m)]} \frac{3\Lambda^4}{4\pi\rho_h} \tag{22}$$

where r_m and r_M are the minimum and maximum radius of each hydrometeor, ρ_h their (constant) density and γ is the incomplete Gamma function [42]. The slope parameter Λ of the size distributions has been parameterized to precipitation rate using a relation $\Lambda = aR^b$ with a and b constant empirical coefficients. The latter has been derived from the Marshall-Palmer PSD (with $\Lambda = 4.1R^{-0.21}$) for raindrops, the Sekhon-Srivastava PSD (with $\Lambda = 2.29R^{-0.45}$) for ice crystals and graupel and the Gunn-Marshall PSD (with $\Lambda = 25.5R^{-0.48}$) for snow aggregates [35]. A Gamma PSD has been chosen for cloud droplets [28]. Radius size ranges of cloud droplets, raindrops, ice graupel, ice crystals and snow have been fixed to 0.001–0.01, 0.1–3.0, 0.1–5, 0.1–1.5, and 0.1–5.0 mm, respectively. Density of ice graupel, ice crystals and snow has been set to 0.5, 0.2 and 0.1 g cm^{-3}, respectively. Snow dielectric constant has been derived by a second-order Maxwell-Garnett formula for inclusions of air in ice matrix. Melting particles have been modeled as water-coated particle with ice core and a coating thickness function of precipitation rate [38].

Microwave gaseous absorption $k_{\rm ag}$ has been here computed by means of the Liebe model [43]. From (1), hydrometeor scattering properties are completely described by k_d, calculated for a hydrometeor mixture within each layer through

$$k_d(\mu_s) = \sum_{h=1}^{N_h} k_{dh}(\mu_s) = \sum_{h=1}^{N_h} \int_{r_{\rm mh}}^{r_{\rm Mh}} \sigma_{dh}(r, \mu_s) N_h(r) dr \tag{23}$$

where σ_{dh} is the differential scattering cross section of the hth hydrometeor. In order to compute σ_{dh} and hydrometeor absorption cross-section σ_{ah}, to a first approximation the hydrometeor shapes have been here assumed all spherical or sphere-equivalent. This implies that the Mie theory can be applied in an efficient way for both homogeneous and spherically-coated inhomogeneous particles [28]. Large raindrops and ice particles cannot verify this assumption, as they may be modeled as needles, plates or dendrites, but the nonsphericity is considered as a second-order effect in our unpolarized RTE model.

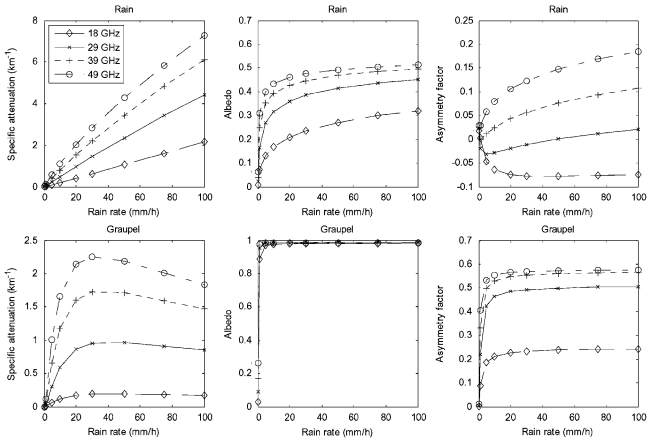

Fig. 6. Optical parameters in terms of specific attenuation (or extinction coefficient) k_e, volumetric albedo w and scattering asymmetry factor g as a function of the precipitation rate for raindrops (top panels) and graupel particles (bottom panels) at 18, 29, 39, and 49 GHz.

Once k_e and k_d are known, the optical parameters can be easily computed for each cloud layer. Fig. 6, shows these optical parameters as a function of rain rate for raindrops and graupel particles at 18.7, 29.5, 39.6, and 49.5 GHz. Results for snow particles are not shown being their behavior quite similar to that of graupel particles with reduced values of k_e (not larger than 1.1 km^{-1} at 49 GHz) and slightly larger values of g (which can reach 0.85 at 49 GHz). Albedo of ice hydrometeors, i.e., graupel and snow, is close to 1 even for low rain-rates, as opposed to that of raindrops which is at most 0.5. However, raindrops exhibit a higher specific attenuation which is, for a given precipitation rate, double than the graupel one (which is, in its turn, almost double than that of snow). The asymmetry factor for graupel and snow is also much higher than that of raindrops which can be even negative at lower frequencies [35]. The radiative implication of these considerations is that raindrop layers will mostly contribute to determine signal fade, while graupel, and, to a minor extent, snow will give rise to incoherent scattering effects weighted by albedo [15].

Formulas to predict rain attenuation have been already proposed [11], [12], but the vertical structure of a rain cloud needs to be described by all optical parameters both for precipitating liquid and ice particles. Previous plots may justify a polynomial regression model of the optical parameters for rain, graupel, and snow hydrometeors

$$\begin{cases} k_e = a_{k0} + \sum_{n=1}^{N=2} a_{kn} R^n \\ w = a_{w0} + \sum_{n=1}^{N=2} a_{wn} R^n \\ g = a_{g0} + \sum_{n=1}^{N=2} a_{gn} R^n \end{cases} \tag{24}$$

where a_{kn}, a_{wn}, and a_{gn} are frequency-dependent regression coefficients and N is the polynomial degree. Numerical tests

TABLE I
REGRESSION COEFFICIENT FOR ESTIMATING RAIN, GRAUPEL AND SNOW SPECIFIC ATTENUATION k_e (km^{-1}), ALBEDO w AND ASYMMETRY FACTOR g FROM SURFACE RAIN-RATE R (mm/h) ADOPTING THE QUADRATIC MODEL AS IN (24) at 12.5, 18.7, 29.6, 39.6, AND 49.5 GHz (SEE TEXT FOR DETAILS). ROOT MEAN SQUARE ERROR (RMSE) IS ALSO INDICATED AND THE VALIDITY OF THE RESULTS IS FOR $R > 1$ mm/h

Hydro meteor	*Freq. (GHz)*	***Specific attenuation k_e***				***Albedo w***				***Asymmetry factor g***			
		a_{k0}	a_{k1}	a_{k2}	*RMSE*	a_{w0}	a_{w1}	a_{w2}	*RMSE*	a_{g0}	a_{g1}	a_{g2}	*RMSE*
	12.5	-1.6806e-2	9.5891e-3	9.3271e-6	3.5896e-3	5.5737e-2	2.2946e-3	-1.1536e-5	3.7233e-3	1.4674e-2	-3.3231e-3	2.1657e-5	9.2357e-3
	18.7	-2.4176e-2	2.1591e-2	3.0029e-6	4.1135e-3	1.1652e-1	4.4684e-3	-2.5091e-5	9.0761e-3	-4.5606e-2	-1.2181e-3	9.7189e-6	5.7749e-3
Rain	*29.6*	-1.8720e-2	5.0491e-2	-6.0645e-5	3.5981e-3	2.5455e-1	4.9266e-3	-3.0524e-5	1.3318e-2	-3.6498e-2	9.0458e-4	3.3059e-6	4.3213e-4
	39.6	4.6018e-2	7.6153e-2	-1.5662e-4	2.4123e-2	3.4206e-1	3.9506e-3	-2.4983e-5	1.1508e-2	3.6047e-3	1.9792e-3	-9.7044e-6	2.8848e-3
	49.5	1.5242e-1	9.5068e-2	-2.4283e-4	4.7740e-2	3.9150e-1	3.1441e-3	-1.9940e-5	9.3422e-3	4.8597e-2	2.7903e-3	-1.4691e-5	4.9642e-3
	12.5	9.5410e-3	1.1635e-3	-9.2454e-6	4.4826e-3	9.3165e-1	1.0909e-3	-7.9216e-6	5.2685e-3	7.9265e-2	7.1949e-4	-5.0374e-6	2.9247e-3
	18.7	4.6298e-2	5.5218e-3	-4.3961e-5	2.1491e-2	9.6955e-1	4.2915e-4	-3.1213e-6	2.0720e-3	1.8278e-1	1.8523e-3	-1.2916e-5	7.3798e-3
Graupel	*29.6*	2.5162e-1	2.6519e-2	-2.1309e-4	1.0675e-1	9.8292e-1	1.5497e-4	-1.1267e-6	7.3457e-4	4.1986e-1	2.7541e-3	-1.9728e-5	1.2235e-2
	39.6	5.8486e-1	4.3271e-2	-3.5776e-4	1.9209e-1	9.8463e-1	7.5530e-5	-5.5158e-7	3.7318e-4	4.9582e-1	2.1784e-3	-1.5352e-5	9.1442e-3
	49.5	9.4596e-1	4.9713e-2	-4.2506e-4	2.4477e-1	9.8405e-1	1.2779e-5	-1.2045e-7	1.3619e-4	5.3143e-1	1.4483e-3	-1.0399e-5	6.4916e-3
	12.5	-2.0452e-3	7.6086e-4	-4.4413e-6	7.4647e-4	8.5638e-1	3.6286e-3	-2.6929e-5	1.9046e-2	8.7062e-2	2.5569e-3	-1.7909e-5	1.0049e-2
	18.7	-6.4774e-3	2.6465e-3	-1.5737e-5	2.8747e-3	9.2604e-1	1.7640e-3	-1.3076e-5	9.2215e-3	1.8293e-1	5.8653e-3	-4.0795e-5	2.2278e-2
Snow	*29.6*	-1.7464e-2	8.9274e-3	-5.3875e-5	1.0568e-2	9.5926e-1	8.6225e-4	-6.3573e-6	4.3622e-3	3.8004e-1	8.9126e-3	-6.3397e-5	3.6905e-2
	39.6	-2.9920e-2	1.7989e-2	-1.0963e-4	2.2456e-2	9.6942e-1	6.0270e-4	-4.4278e-6	2.9798e-3	5.2460e-1	7.8870e-3	-5.6725e-5	3.4715e-2
	49.5	-4.1350e-2	2.9460e-2	-1.8095e-4	3.8425e-2	9.7452e-1	4.6828e-4	-3.4238e-6	2.2905e-3	6.2416e-1	6.6035e-3	-4.7694e-5	2.9732e-2

have proved that a quadratic form with $N = 2$ in (24) is a better choice than a power-law model for all three optical parameters (especially w and g) between *Ku* and *V* band. Table I provides the regression coefficients of (24) and the related estimate accuracy for each precipitating hydrometeor for $R > 1$ mm/h and between 12 and 50 GHz. The estimation error tends to increase for rain-rates smaller than few millimeters per hour and larger than $\sim$60 mm/h due to the quadratic form of (24).

C. Numerical Results and Comparison With ITALSAT Data

Using (24) we can basically transform the hydrometeor content profiles into microwave optical parameters. The other RTE input parameters, that we need to specify, are: *i*) the beacon frequency ν; *ii*) the observation angle θ; *iii*) the surface emissivity e_s. With respect to item *i*), we have selected typical satellite link frequencies. The analysis has included the frequency bands of OLYMPUS and ITALSAT beacons, i.e., 12.5, 18.7, 29.7, 39.6, and 49.5 GHz [2], and the most common channel frequencies of ground-based radiometers, that is at 13.0, 20.6, 22.3, 23.8, 31.7, 36.5, 50.2, 53.8 GHz, and 90 GHz in order to characterize the entire spectrum of interest [19]. With respect to item *ii*), we have considered all zenith angles for ground-based antennas, but for brevity we will show only the intermediate case of 45° observation angle. As proved, the validity of the sky-noise Eddington model is not limited by neither frequency nor angle variation. With respect to item *iii*), we have set the Lambertian emissivity $e_{\rm sL}$ to 0.95 as a microwave average value of land surfaces.

Finally, by using the coupled rain-cloud radiative transfer model illustrated before, a large simulated data set, consisting of 30 000 cloud structures together with related columnar hydrometeor contents, surface rain-rate, slant-path attenuations and received sky-noise temperatures at given frequencies and observation angles, has been simulated assuming a surface temperature between 5° and 30°C. Fig. 7, shows the slant-path attenuation $A_s = Asec\theta$ [see (3) and Fig. 1] at 45° elevation angle and at 18.7 and 49.5 GHz, simulated from the cloud structure ensemble shown in Fig. 5, for Ns and Cb genera as function of the surface rain-rate. Results are also plotted in terms of the difference $A_s - A_{\rm liquid}$ where $A_{\rm liquid}$ refers to the case where only liquid hydrometeors (i.e., cloud droplets and raindrops) are taken into account. A fairly high correlation is noted between slant path attenuation and both rain-rate and columnar water content. As expected, total path attenuation increases with frequency for a given surface rainfall. At 49 GHz, slant path attenuations larger than 50 dB are obtained for rainfall less than 40 mm/h. The significant role of precipitating ice hydrometeors in determining total attenuation is appreciated for convective rain at 49 GHz, where neglecting precipitating ice can give rise to an underestimation of tens of decibels. This should not surprise if, from Fig. 6, we look at the values of graupel extinction which can be up to 2 km^{-1} at 49.5 GHz. The underestimation is lower for stratiform rain due to the smaller contents of precipitating ice associated to lower rain-rates, as from Fig. 5.

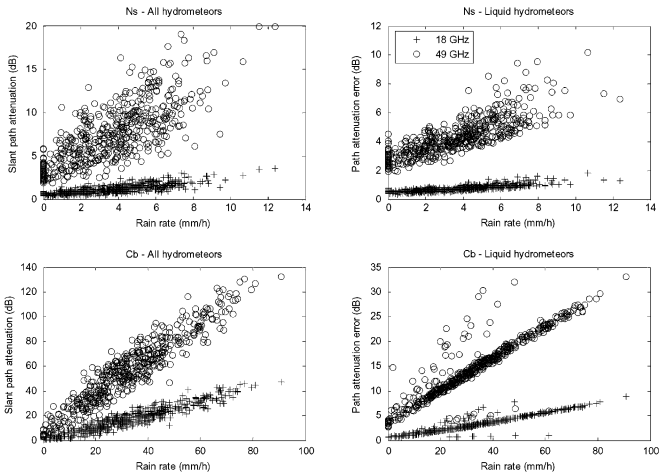

Fig. 7. Slant-path attenuation A_s at 45° elevation angle and at 18 and 39 GHz, simulated from the cloud structure ensemble shown in Fig. 5, for Ns (top panels) and Cb genera (bottom panels) as function of the surface rain-rate. Left panels refer to the case where all hydrometeors are considered, while right panels show to the errors $(A_s - A_{\rm liquid})$ due to case where only liquid hydrometeors (i.e., cloud droplets and raindrops) are taken into account.

Fig. 8 shows the ground-based brightness temperature at 45° zenith angle and at 18.7 and 49.5 GHz, simulated from the same cloud structure ensemble for Ns and Cb genera as a function of rain-rate. The stronger the rain regime is the more pronounced

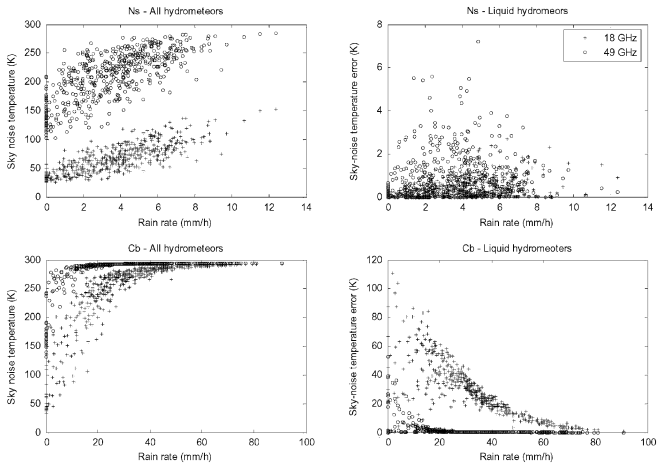

Fig. 8. Ground-based sky noise temperature T_B at 45° zenith angle and at 18 and 49 GHz over a Lambertian land surface, simulated from the cloud structure ensemble shown in Fig. 2, for Ns (top panels) and Cb genera (bottom panels) as function of surface rain-rate when considering all hydrometeors (left panels) and the corresponding errors ($T_B - T_{B\mathrm{liquid}}$) when considering only liquid hydrometeors (right panels).

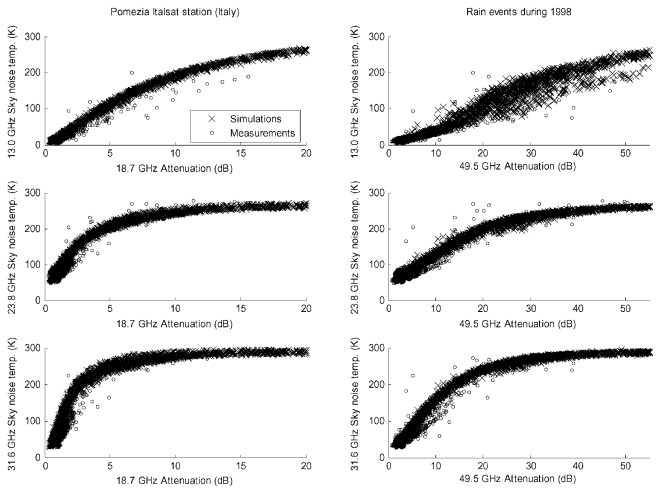

Fig. 9. Ground-based sky noise temperature at 13, 23.8, and 31.6 GHz against slant path attenuation at 18.7 and 49.5 GHz, measured at 41.8° elevation angle at the ITALSAT station of Pomezia (Rome, Italy) during 5 rainfall events on 1998 and compared with simulations derived from the sky-noise delta-Eddington model applied to synthetic rain clouds as those in Fig. 5.

is the saturation of T_B's as a function of rainfall rate and, consequently, path attenuation. For Ns a saturation effect is noted only for very large rain rates. For convective rainfall, the frequency dependence is largely reduced for rain-rate larger than 40 mm/h (path attenuation larger than 15 dB or columnar water larger than 4 kg/m^2) being the asymptotic values of T_B's quite similar. Precipitating ice hydrometeors play a role also in determining ground-based T_B's due to their impact on multiple scattering effects [8], [22]. If only liquid hydrometeors are considered to compute $T_{B\mathrm{liquid}}$, as in Fig. 7 for A_{liquid}, there is an overall underestimation of T_Bs (i.e., $T_B - T_{B\mathrm{liquid}} > 0$) which may be negligible (less than few percent) for Ns, but significant (up to 20%) for Cb at lower rain-rates and frequencies when the atmosphere is still relatively optically thin [39].

The main advantage of dealing with a physically-based propagation modeling tool is the capability to reproduce any configuration of the instrumental equipment at microwave and millimeter-wave. An experimental verification of the sky-noise Eddington model simulations should be carried out by employing a receiver whose antenna noise temperature can be independently evaluated. A way to circumvent this problem is to use measurements derived from co-located link receivers and microwave radiometers, possibly working within frequency bands close to each other and with a similar pointing angle. In this work path attenuation data acquired at the ITALSAT-satellite ground-station, located in Pomezia (Rome, Italy), have been used [2]. Since April 1994 measurements of the three ITALSAT-F1 propagation beacons at 18.7, 39.6, and 49.5 GHz have been performed every second at an elevation angle of 41.8 degrees with a three-reflector receiving antenna having the main dish diameter of 3.5 m (that is, beam-widths from 0.2° to 0.5°). The ground station was measuring the amplitude and phase of co-polar and cross-polar signals, at 18.7 and 39.6 GHz, and the polarization transfer matrix of the atmosphere at 49.5 GHz. Concurrent measurements performed by two microwave radiometers (REC-1 and REC-2) at 13.0, 23.8, and 31.6 GHz, pointed to the ITALSAT satellite with beam-widths between 2° and 4°, and a set of ground meteorological instruments also including a tipping bucket rain gauge, have been synchronously logged every 4 s by the ITALSAT ground station. The radiometric data have been routinely used to assess the clear-air atmospheric reference level for calibrating the ITALSAT beacon clear-air path attenuation. A moving average with 1-minute window and 1-minute sampling period has been applied to analyze raw data.

In order to show a robust test, we have selected five cases of both moderate and intense rainfall, observed in Pomezia during 1998. Fig. 9 shows the ground-based sky noise temperature at 13, 23.8, and 31.6 GHz against slant path attenuation A_s at 18.7 and 49.5 GHz measured at 41.8° elevation angle at the ITALSAT station of Pomezia (Rome, Italy) during 5 rainfall events on 1998 and compared with simulations derived from the sky-noise delta-Eddington model applied to synthetic rain clouds as those in Fig. 5. The case studies refer to Nov. 19, 1997 at 09:00 local mean time (LMT), Apr. 27, 1998 at 10:00 LMT, Apr. 29, 1998 at 17:00 LMT, May 03, 1998 at 17:00 LMT and Aug. 28, 1998 at 06:00 LMT. By collecting all the events, more than 500 minutes of rain observations have been selected. The convective rain events of Apr. 29, 1998 and Aug. 28, 1998, which lasted only few hours, exhibit path attenuation up to 50 dBs at 49.5 GHz with a large dynamics of the measured radiometric brightness temperature up 290 K at 31.6 GHz. It is worth mentioning that Fig. 9 is not aimed at performing a comparison "point by point" between simulations and measurements as we did not try to "reproduce" the radiometric measurements by model tuning, but to show how multi-frequency attenuation and sky-noise data, derived from a large set of measurements, are represented by SNEM simulations.

Path attenuation and sky-noise temperature simulations have been derived by merging the results from middle and winter seasons with surface temperatures going from 15 to 30°C, as deduced from meteorological station data acquired during each event. From Fig. 9 it can be appreciated the ability

of SNEM synthetic data to follow the dynamics and mutual correlation between attenuation and radiometric data spanning from 13.0 to 49.5 GHz (similar results have been obtained at 39.6 GHz). There is a tendency of sky-noise simulated data to overestimate corresponding measurements for intermediate values of path attenuation and higher frequency plots (as for T_B at 31.6 GHz versus A_s at 49.5 GHz). Hydrometeor depolarization effects, residual inter-calibration errors and different beam-widths of the two different instruments (satellite receiver and microwave radiometer) may affect this intercomparison. In particular, the antenna-field-of-view may be not completely filled with hydrometeors as assumed within SNEM simulations, a condition often called "beam-filling" error. This effect is more pronounced for less directive antennas as in the case of low-frequency radiometer beams at 13.0 GHz. Nevertheless, the nonlinear behavior of T_B versus A_s is clearly captured and highest values of slant-path attenuation at 49 GHz are fairly well represented by simulated sky-noise temperature data.

IV. Conclusion

An analytical model, called sky-noise Eddington model (SNEM), for characterizing antenna noise temperature due rain clouds has been described. In case of a homogeneous atmosphere, the closed-form solution has been obtained by the expansion of the brightness temperature angular spectrum in terms of Legendre polynomials, as suggested by Edddington's approximation. For a vertically stratified atmosphere, an explicit recursive solution has been set up with appropriate boundary conditions, parameter scaling transformation and a stable inversion procedure. The accuracy of SNEM has been systematically evaluated by comparing it with an accurate numerical solution in terms of T_B and not of fluxes, as usually done in literature. The expected errors for a rain slab model fall below 1.5% for both ground-based and satellite-based antennas. The delta-Eddington transformation of the optical parameters plays a crucial role in SNEM and it should be always used for antenna noise simulations. The effect of the antenna pattern has been also evaluated showing that, for ground-based observations, it is generally negligible due to the angularly-smoothed radiometric response to rain, especially at high frequencies.

A physically-oriented radiative cloud model, able to characterize the sky noise temperature and path attenuation, has been also introduced. Nimbostratus and cumulonimbus models have been derived from a physical-statistical technique, previously developed. For a large set of beacon channel frequencies quadratic regression relations have been derived for specific attenuation, albedo and asymmetry factor for precipitating sphere-equivalent hydrometeors (raindrops, graupel particles and snow aggregates). Finally, simulations obtained from the physically-based SNEM algorithm have been compared with attenuation and radiometric data, acquired at the ITALSAT station of Pomezia during 5 rainfall events on 1998, showing a fairly good agreement both for dynamic range and nonlinear correlation behavior.

It is worth mentioning that the validity of the proposed SNEM approach is not limited, in principle, to microwave and millimeter-wave applications through Earth's atmosphere, but could be applied to a generic random medium such as vegetation cover. An apparent limitation of the proposed SNEM scheme is the assumption of a planar stratified medium which might be adequate in some observational circumstances such as convective rain cells. This hypothesis should be verified by comparing the horizontal size of the scattering phenomenon with the antenna beam-width. If the beam-width is relatively narrow, as for ground-based antennas, the proposed model could be used by considering a slanted geometry [22]. Finally, SNEM algorithm cannot be applied to simulate polarized T_B measurements, but more complicate schemes should be employed (e.g., [44]). Indeed, if each term of scattering phase matrix in a linearly-polarized basis may be expanded in Legendre polynomial and truncated at 1st order, then the Eddington theory would be applicable in a straightforward way. Even the surface may be supposed polarized if no depolarization is included. If this is not the case, we would loose the effectiveness of a closed-form solution. We stress that, when dealing with nonisotropic media, other degrees of freedom become significant such as the particle axial-ratio and their random orientation. The need to specify these parameters very often leads to significant unrealistic errors which may be much larger than those due to a more conservative choice of sphere-equivalent particles. Future developments shall deal with radio propagation applications by introducing prediction methods based on a multiple regression analysis and modeling the frequency and elevation-angle T_B scaling for stratiform and convective rainfall.

Appendix A
The Sky-Noise Eddington Model (SNEM)

Let us consider the special case of Fig. 1 consisting of a uniform atmospheric slab ($L = 1$). By substituting the Eddington expansion for both T_B and p_a, given in (8) and (9), into (4) and solving the integral of J, it holds

$$\mu\frac{dT_{B0}(\tau)}{d\tau}+\mu^2\frac{dT_{B1}(\tau)}{d\tau}=-T_{B0}(\tau)-\mu T_{B1}(\tau)+J_E(\tau,\mu) \tag{A.1}$$

where J_{E} represents the Eddington approximation of the source function J, given by

$$J_E(\tau,\mu)=w[T_{B0}(\tau)+g\mu T_{B1}(\tau)]+(1-w)(t_0+t_1\tau) \tag{A.2}$$

Notice that the layer temperature $T(\tau)$ in (A.2) has been supposed to be linearly dependent on τ with coefficients t_0 and t_1 given by

$$\begin{aligned} T(\tau)=t_0+t_1\tau&=T(0)+\left[\frac{T(\tau_s)-T(0)}{\tau_s}\right]\tau \\ &=T(0)+\frac{\Gamma_T}{k_e}\tau \end{aligned} \tag{A.3}$$

where Γ_T is the vertical temperature positive gradient (or thermal lapse rate) and H is the layer vertical thickness. Integrating between -1 and 1 the differential equation (A.1), multiplied first by $P_0(\mu)$ and then by $P_1(\mu)$, and using the orthogonal property of Legendre polynomials, the differential equation (A.1) reduces to the following system of ordinary

differential equations with constant coefficients, conveniently put in a matrix form:

$$\frac{d}{d\tau}\begin{bmatrix} T_{B0}(\tau) \\ T_{B1}(\tau) \end{bmatrix} = \begin{bmatrix} 0 & -(1-wg) \\ -3\,(1-w) & 0 \end{bmatrix} \begin{bmatrix} T_{B0}(\tau) \\ T_{B1}(\tau) \end{bmatrix} + \begin{bmatrix} 0 \\ 3(1-w)(t_0+t_1\tau) \end{bmatrix}. \quad \text{(A.4)}$$

The solution of the associated homogeneous differential equation of (A.4) can be found by using the conventional eigenanalysis method, yielding

$$\begin{bmatrix} T_{B0}(\tau) \\ T_{B1}(\tau) \end{bmatrix}_H = C_1 \begin{bmatrix} 1 \\ c \end{bmatrix} e^{-\lambda\tau} + C_2 \begin{bmatrix} 1 \\ -c \end{bmatrix} e^{\lambda\tau} \quad \text{(A.5)}$$

where C_1 and C_2 are the integration constants. The eigenvalues $\pm\lambda$ and the constant c are given by

$$\lambda = \sqrt{3(1-wg)(1-w)}, \quad c = \sqrt{\frac{3(1-w)}{1-wg}}. \quad \text{(A.6)}$$

The structure of the known vector suggests looking for a particular solution which is a two-parameter linear function of τ. Substituting this unknown function into (A.4), the particular solution is found to be

$$\begin{bmatrix} T_{B0}(\tau) \\ T_{B1}(\tau) \end{bmatrix}_P = \begin{bmatrix} t_0 \\ -t_1/(1-wg) \end{bmatrix} + \begin{bmatrix} t_1 \\ 0 \end{bmatrix} \tau. \quad \text{(A.7)}$$

The general solution of (A.4) is then

$$\begin{cases} T_{B0}(\tau) = C_1 e^{\lambda\tau} + C_2 e^{-\lambda\tau} + t_0 + t_1\tau \\ T_{B1}(\tau) = cC_1 e^{\lambda\tau} - cC_2 e^{-\lambda\tau} - \frac{t_1}{1-wg}. \end{cases} \quad \text{(A.8)}$$

The integration constants C_1 and C_2 can be derived by imposing the boundary conditions for T_{B0} and T_{B1}. These constants can be obtained by prescribing the general boundary in terms of upwelling and downwelling flux densities F_- and F_+, defined respectively by

$$\begin{cases} F_-(\tau) = 2\pi \int_{-1}^{0} T_B(\tau,\mu)\mu d\mu = \pi\left[-T_{B0}(\tau) + \frac{2}{3}T_{B1}(\tau)\right] \\ F_+(\tau) = 2\pi \int_{0}^{1} T_B(\tau,\mu)\mu d\mu = \pi\left[T_{B0}(\tau) + \frac{2}{3}T_{B1}(\tau)\right]. \end{cases} \quad \text{(A.9)}$$

where (9) has been used in (A.9). In terms of $F_?$ and F_+ for a Lambertian boundary condition, given in (7), it holds, please see (A.10) at the bottom of the page. Inserting the expressions of T_{B0} and T_{B1} into previous equations, after some algebraic manipulation, the following linear equation system is deduced for C_1 and C_2 in (A.11), shown at the bottom of the page. The previous linear system can be solved either analytically in the simple case of a single layer or numerically. It is worth noting that the matrix to be inverted on the left-hand side of (A.11) contains exponentials with a positive argument whose values, for a large optical thickness, can give rise to unexpected ill-conditioning in the inversion procedure [36]. In order to tackle this problem, a scaling transformation of the unknowns C_1 and C_2 can be performed by exploiting the structure of the matrix itself. If we let $\tau_0 = 0$ and define [10]

$$\begin{bmatrix} C_1 \\ C_2 \end{bmatrix} \equiv \begin{bmatrix} \tilde{C}_1 e^{\lambda\tau_0} \\ \tilde{C}_2 e^{-\lambda\tau_s} \end{bmatrix} = \begin{bmatrix} \tilde{C}_1 \\ \tilde{C}_2 e^{-\lambda\tau_s} \end{bmatrix} \quad \text{(A.12)}$$

then the linear system (A.12) becomes

$$\begin{bmatrix} c_{11} & c_{12}e^{-\lambda\tau_s} \\ c_{21}e^{-\lambda\tau_s} & c_{22} \end{bmatrix} \begin{bmatrix} \tilde{C}_1 \\ \tilde{C}_2 \end{bmatrix} = \begin{bmatrix} d_1 \\ d_2 \end{bmatrix} \quad \text{(A.13)}$$

where the terms c_{ij} and $d_i\,(i = 1, 2)$ are clearly identified by comparing (A.13) with (A.11). The system (A.13) is now inconditionally stable for any optical thickness value and its solution can provide the unknown constants C_1 and C_2. By coupling (A.8) and (A.14), once the physical and optical parameters of the atmospheric layer are known, the RTE can be analytically solved using (9).

A limitation of the Eddington model is due to the first-order expansion of the azimuthally-averaged scattering phase function in (8), which may be inadequate for strongly scattering conditions when $g > 0.5$, e.g., in presence of precipitating ice within a rainfall cloud (see Fig. 6) [30]. In order to extend the validity of (A.8), a *delta-Eddington* approach can be adopted extending it from radiance flux to T_B calculations [23]. Following this approach, the truncated *delta-Eddington* phase function p_δ is defined as an approximation of the phase function p including a forward scatter peak through a Dirac delta function δ and a two-term Legendre expansion of p itself, that is [30]

$$p_\delta(\mu_s) \equiv 2f\delta(1-\mu_s) + (1+3g'\mu_s) - f(1+3g'\mu_s) \quad \text{(A.14)}$$

where f is, by definition, the fraction of forward scattering peak and g' is the asymmetry factor of p_δ. Note that p_δ is correctly normalized to 4 π. The new factors f and g' can be determined by imposing the values of the first and second moments of the *delta-Eddington* phase function p_δ. If p_δ is required to have the same asymmetry factor g as the original phase function p, g' is determined once f is known. The value of f may be obtained by imposing, for instance, that the second moment of p_δ is equal to the second moment of p, approximated by the Heyney-Greenstein analytical phase function [34]. A mentioned property of the Heyney-Greenstein phase function is that its nth moment is equal to nth power of g and it represents a fairly good approximation of the Mie numerical phase function [15]. Thus, f can be determined resulting $f = g^2$ and then $g' = g/(1+g)$.

$$\begin{cases} T_{B0}(0) + \frac{2}{3}T_{B1}(0) = T_c \\ T_{B0}(\tau_s) - \frac{2}{3}T_{B1}(\tau_s) = e_{\rm sL}T_S + (1-e_{\rm sL})\left[T_{B0}(\tau_s) + \frac{2}{3}T_{B1}(\tau_s)\right] \end{cases} \quad \text{(A.10)}$$

$$\begin{bmatrix} 1+\frac{2}{3}c & 1-\frac{2}{3}c \\ e_{\rm sL}e^{-\lambda\tau_s} - \frac{2}{3}(2-e_{\rm sL})ce^{-\lambda\tau_s} & e_{\rm sL}e^{\lambda\tau_s} + \frac{2}{3}(2-e_{\rm sL})ce^{\lambda\tau_s} \end{bmatrix} \begin{bmatrix} C_1 \\ C_2 \end{bmatrix} = \begin{bmatrix} T_{\rm c} - t_0 + \frac{2}{3}\frac{t_1}{(1-wg)} \\ e_{\rm sL}T_S - e_{sL}(t_0+t_1\tau_s) - (2-e_{\rm sL})\frac{2}{3}\frac{t_1}{(1-wg)} \end{bmatrix} \quad \text{(A.11)}$$

As a final step, it is possible to evaluate the consequences of using the *delta-Eddington* phase function p_δ by inserting the latter into the azimuthally-averaged RTE. It is readily deduced that the *delta-Eddington RTE* for T_B is formally identical to the original RTE, given in (4), if the optical parameters τ, w, and g are modified into τ', w', and g' by

$$\tau' = (1 - wg^2)\tau, \quad w' = \frac{(1-g^2)w}{1-wg^2}, \quad g' = \frac{g}{1+g}. \quad \text{(A.15)}$$

Previous expressions in (A.15) can be interpreted as a similarity transformation in RTE. Note that the transformed asymmetry factor g' can be at most 0.5 when $g = 1$. The numerical results of Section II will show the significant impact of using the *delta-Eddington* approach in terms of RTE accuracy.

Appendix B
Extension to Satellite-Based Antennas

For satellite-based antennas, the argumentation is analogous to that illustrated for ground-based antennas. The upwelling $T_B(0, -\mu_0)$, observed at $\tau = 0$ (see Fig. 1) is given by

$$T_B(0,-\mu_0) = T_B(\tau_s,-\mu_0)e^{-\tau_s/\mu_0} + \frac{1}{\mu_0}\int_0^{\tau_s} J(\tau,-\mu_0)e^{-\tau/\mu_0}d\tau. \quad \text{(B.1)}$$

Note that for a Fresnelian boundary condition, useful to characterize a sea surface background from satellite, the azimuthally-isotropic surface boundary condition can be formulated as

$$T_B(\tau_s,-\mu_0) = e_{\rm sF}(\mu_0)T_s + [1 - e_{\rm sF}(\mu_0)]T_B(\tau_s,\mu_0) \quad \text{(B.2)}$$

where $e_{\rm sF}$ is the Fresnelian surface emissivity, dependent on μ_0 and on the polarization state. Indeed, the surface emissivity of a partially-rough surface (such as land including relief effects and ocean with foam) can be also treated by decomposing e_s into a properly weighted specular Fresnelian component $e_{\rm sF}$ and a diffused Lambertian component $e_{\rm sL}$ [38].

After the evaluation of the integral (B.1) using (A.2), the SNEM closed-form approximation of upwelling T_B at the top of the atmosphere for a single homogeneous layer is

$$\begin{aligned} T_B(0,-\mu_0) = {} & T_B(\tau_s,-\mu_0)e^{-\tau_s/\mu_0} \\ & + \left[t_0 + t_1\mu_0 + \frac{wg\mu_0}{(1-wg)}t_1\right] \\ & \times (1 - e^{-\tau_s/\mu_0}) - t_1\tau_s e^{-\tau_s/\mu_0} \\ & + wC_1\frac{1 - c\mu_0 g}{1+\lambda\mu_0}\left[1 - e^{-(\tau_s/\mu_0)-\lambda\tau_s}\right] \\ & + wC_2\frac{1 + c\mu_0 g}{1-\lambda\mu_0}\left[1 - e^{-(\tau_s/\mu_0)+\lambda\tau_s}\right] \end{aligned} \quad \text{(B.3)}$$

where $T_B(\tau_{\rm s}, -\mu_0)$ is given by inserting (11) into the surface boundary condition (B.2) and, again, the optical parameters τ_s, w, and g may be transformed by *delta-Eddington* similarity equations given by (A.15).

Fig. 10 shows the same as in Fig. 2, but for satellite-based antennas. The comparison with the ground-based antenna case indicates smaller values of the percentage errors ranging up 15% even though the delta-Eddington transform is not applied. In a way, looking at the final expression given in (B.3), we realize that the upwelling T_B is computed having as a boundary the dowelling T_B. This means that the discrepancy with respect to the exact DisORT solution is further reduced by using this "two-way" radiance formulation. In other words, the extinction processes become dominant with respect to the multiple-scattering source processes when the scenario is observed from top of the medium. When applying the delta-Eddington transformation, as expected, the overall percentage errors are further reduced. Their values are confined within 2% even when considering the overall independent variability of the optical parameters and viewing angles.

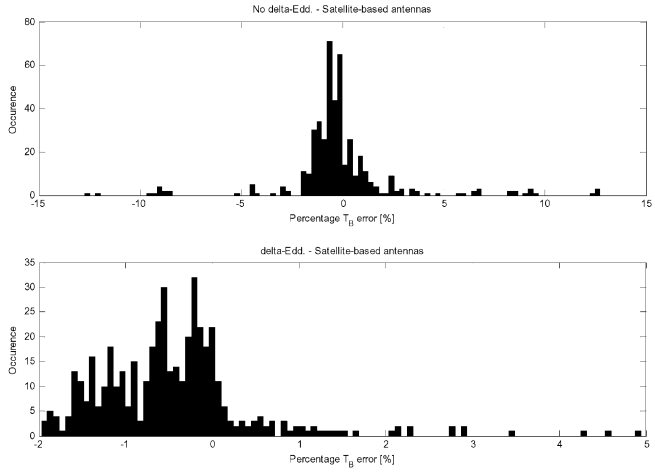

Fig. 10. Same as in Fig. 2, but for satellite-based antennas at nadir.

Previous expressions can be sky-noise to a stratified atmosphere, as in Fig. 1, using the same recursive approach as in (18). The set of recursive equations to determine the upwelling $T_B(\tau_{l-1}, -\mu_0)$ at the $(l-1)$th atmospheric level τ_{l-1} is then the following:

$$\begin{aligned} & T_B(\tau_L,-\mu_0) = e_{\rm sF}(\mu_0)T_s + [1 - e_{\rm sF}(\mu_0)]T_B(\tau_L,\mu_0) \\ & T_B(\tau_{l-1},-\mu_0) = T_B(\tau_l,-\mu_0)e^{-(\tau_l-\tau_{l-1})/\mu_0} \\ & \quad + \left[t_{0l} + t_{1l}\mu_0 + \frac{w_l g_l \mu_0}{(1-w_l g_l)}t_{1l}\right]\left[1 - e^{-(\tau_l-\tau_{l-1})/\mu_0}\right] \\ & \quad - t_{1l}[\tau_l - \tau_{l-1}e^{-(\tau_l-\tau_{l-1})/\mu_0}] \\ & \quad + w_l C_{1l}\frac{1 - c_l\mu_0 g_l}{1+\lambda_l\mu_0}e^{-\lambda_l(\tau_l-\tau_{l-1})} \\ & \quad \times [e^{\lambda_l(\tau_l-\tau_{l-1})} - e^{-(\tau_l-\tau_{l-1})/\mu_0}] \\ & \quad + w_l C_{2l}\frac{1 + c_l\mu_0 g_l}{1-\lambda_l\mu_0}e^{\lambda_l(\tau_l-\tau_{l-1})} \\ & \quad \times \left[e^{-\lambda_l(\tau_l-\tau_{l-1})} - e^{-(\tau_l-\tau_{l-1})/\mu_0}\right] \end{aligned} \quad \text{(B.4)}$$

where $l = L, L-1, \ldots, 1$ and upwelling $T_B(\tau_s = \tau_L, -\mu_0)$ at the surface is obtained from downwelling $T_B(\tau_s = \tau_L, \mu_0)$ by applying the boundary condition (B.2) at $\tau_l = \tau_L$.

Acknowledgment

The author gratefully acknowledges Dr. E. Fionda, Mr. F. Consalvi, FUB, Rome, and Dr. A. Martellucci, ESA, The Netherlands, for providing ITALSAT data. An anonymous reviewer is thanked for very helpful comments and suggestions.

REFERENCES

[1] D. V. Rogers, L. J. Ippolito Jr., and F. Davarian, "System requirements for Ka-band propagation effects on earth-satellite links," *Proc. IEEE*, vol. 85, pp. 810–821, 1997.

[2] B. R. Arbesser-Rastburg and A. Paraboni, "European research on Ka-band slant path propagation," in *Proc. IEEE*, vol. 85, 1997, pp. 843–852.

[3] M. Filip and E. Vilar, "Optimum utilization of the channel capacity of a satellite link in the presence of amplitude scintillations and rain attenuation attenuation," *IEEE Trans. Commun.*, vol. 38, pp. 1958–1965, 1990.

[4] P. A. Watson and Y. F. Hu, "Prediction of attenuation on satellite-earth links for systems operating with low fade margins," in *Proc. Inst. Elect. Eng.—Microw. Antennas Propagat.*, vol. 141, 1994, pp. 467–472.

[5] A. Dissanyake, J. Allnut, and F. Haidara, "A prediction model that combines rain attenuation and other propagation impairments along earth-satellite paths," *IEEE Trans. Antennas Propag.*, vol. 45, pp. 1546–1558, 1997.

[6] M. S. Alouini, S. A. Borgsmiller, and P. G. Steffes, "Channel characterization and modeling for Ka-band very small aperture terminals," *Proc. IEEE*, vol. 85, no. 6, pp. 981–997, 1997.

[7] B. Gremont and M. Filip, "Spatio-temporal attenuation model for application to fade mitigation techniques," *IEEE Trans. Antennas Propag.*, vol. 52, no. 5, pp. 1245–1256, 2004.

[8] A. Ishimaru and R. L.-T. Cheung, "Multiple-scattering effect on radiometric determination of rain attenuation at millimeter-wavelengths," *Radio Sci.*, vol. 15, pp. 507–516, 1980.

[9] C. Catalan and E. Vilar, "Symultaneous analysis of downlink beacon dynamics and sky brightness temperature—Part I: Remote sensing of a slant path," *IEEE Trans. Antennas Propag.*, vol. 50, pp. 524–534, 2002.

[10] F. S. Marzano, C. Di Ciero, P. Ciotti, and E. Fionda, "Characterization of ground-based antenna noise temperature due to precipitating clouds from Ku to W band," in *Proc. CLIMPARA-2001, Budapest (H)*, May, 28–30 2001.

[11] R. L. Olsen, D. V. Rogers, and D. B. Hodge, "The aR^b relationship in the calculation of rain attenuation," *IEEE Trans. Antennas Propag.*, vol. 26, no. 2, pp. 318–329, 1978.

[12] L. Der-Phone and C. Hsing-Yi, "An empirical formula for the prediction of rain attenuation in frequency range 0.6–100 GHz," *IEEE Trans. Antennas Propag.*, vol. 50, pp. 545–551, 2002.

[13] International Telecommunication Union—Radio-Propagation (ITU-R) (2001).

[14] A. Ishimaru, R. Woo, J. W. Armstrong, and D. C. Blackman, "Multiple scattering calculations of rain effects," *Radio Sci.*, vol. 17, pp. 1425–1433, 1982.

[15] F. S. Marzano and L. Roberti, "Numerical investigation of intense rainfall effects on coherent and incoherent slant-path propagation at K band and above," *IEEE Trans. Antennas Propag.*, vol. 41, no. 5, pp. 965–977, 2003.

[16] R. K. Crane, X. Wang, D. B. Westenhaver, and W. J. Vogel, "ACTS propagation experiment: Experiment design, calibration, and data preparation and archival," in *Proc. IEEE*, vol. 85, 1997, pp. 863–878.

[17] R. Polonio and C. Riva, "ITALSAT propagation experiment at 18.7, 39.6, and 49.5 GHz at Spino d'Adda: three years of CPA statistics," *IEEE Trans. Antennas Propag.*, vol. 46, pp. 631–635, 1998.

[18] G. Brussaard, "Radiometry. A Useful Prediction Tool?,", Nordwijk, The Netherlands, European Space Agency Rep. SP-1071, 1985.

[19] E. R. Westwater, J. B. Snider, and M. J. Falls, "Ground-based radiometric observation of atmospheric emission and attenuation at 20.6, 31.75, and 90.0 GHz: A comparison of measurements and theory," *IEEE Trans. Antennas Propag.*, vol. 38, pp. 1569–1580, 1990.

[20] F. S. Marzano and C. Riva, "Cloud-induced effects on long-term amplitude scintillation along millimeter-wave slant paths," *IEEE Trans. Antennas Propag.*, vol. 51, pp. 880–887, 2003.

[21] A. Ishimaru and R. L.-T. Cheung, "Multiple scattering effects on wave propagation due to rain," *Ann. Telecommun.*, vol. 35, pp. 373–379, 1980.

[22] F. S. Marzano, E. Fionda, and P. Ciotti, "Simulation of radiometric and attenuation measurements along earth-satellite links in the 10- to 50-GHz band through horizontally-finite convective raincells," *Radio Sci.*, vol. 34, pp. 841–858, 1999.

[23] F. S. Marzano, G. Ferrauto, and L. Roberti, "Model-based evaluation of antenna noise temperature due to rainclouds at microwave and millimeterwave," in *Proc. 9th Ka Band Conf.*, Ischia, Italy, Nov. 5–7, 2003, pp. 115–122.

[24] K. Stamnes, S. Tsay, W. Wiscombe, and K. Jayaweera, "Numerically stable algorithm for discrete-ordinate-method radiative transfer in multiple scattering and emitting layered media," *Appl. Optics*, vol. 27, pp. 2502–2509, 1988.

[25] J. A. Coakley and P. Chylek, "The two stream approximation in radiative transfer: Including the angle of the incident radiation," *J. Atmos. Sci.*, vol. 32, pp. 409–418, 1974.

[26] M. D. King and H. Harshvardhan, "Comparative accuracy of selected multiple scattering approximations," *J. Atmos. Sci.*, vol. 43, pp. 784–801, 1986.

[27] P. Maral and M. Bousquet, *Satellite Communications*. New York: Academic Press, 2001.

[28] A. Ishimaru, *Wave Propagation and Scattering in Random Media*. New York: Academic Press, 1978, vol. 1 and 2.

[29] G. Brussaard and P. A. Watson, *Atmospheric Modeling and Millimeter Wave Propagation*, London, U.K.: Chapman & Hall, 1995.

[30] J. H. Joseph, W. J. Wiscombe, and J. A. Weinman, "The delta eddington approximation for radiative flux transfer," *J. Atmos. Sci.*, vol. 33, pp. 2452–2459, 1976.

[31] R. Wu and J. A. Weinman, "Microwave radiances from precipitating clouds containing aspherical ice, combined phase, and liquid hydrometeors," *J. Geophys. Res.*, vol. 89, pp. 7170–7178, 1984.

[32] V. V. Sobolev, *Light Scattering in Planetary Atmospheres*. New York: Pergamon, 1975.

[33] W. J. Wiscombe and J. H. Joseph, "The range of validity of the eddington approximation," *Icarus*, vol. 32, pp. 362–377, 1977.

[34] L. G. Heyney and J. L. Greenstein, "Diffuse radiation in the galaxy," *Astrophys*, vol. 93, pp. 70–83, 1941.

[35] A. Gasiewskii, "Microwave radiative transfer in hydrometeors," in *Atmospheric Remote Sensing by Microwave Radiometry*, M. A. Jansen, Ed. New York: Wiley, 1993, ch. 3.

[36] K. S. Roy and A. Swanson, "A new look at the dicrete ordinate method for radiative transfer calculations in anisotropically scattering atmospheres," *J. Atmos. Sci.*, vol. 38, pp. 387–399, 1981.

[37] R. R. Rogers, *A Short Course in Cloud Physics*, 2nd ed. New York: Pergamon Press, 1979.

[38] G. d'Auria, F. S. Marzano, N. Pierdicca, R. P. Nossai, P. Basili, and P. Ciotti, "Remotely sensing cloud properties from microwave radiometric observations by using a modeled cloud database," *Radio Sci.*, vol. 33, pp. 369–392, 1998.

[39] F. S. Marzano, J. Turk, P. Ciotti, S. Di Michele, and N. Pierdicca, "Potential of combined spaceborne microwave and infrared radiometry for near real-time rainfall attenuation monitoring along earth-satellite links," *Int. J. Satell. Commun.*, vol. 19, no. 4, pp. 385–412, 2001.

[40] A. S. Eddington, "On the radiative equilibrium of stars," *Mon. Not. Royal Astronom. Soc.*, vol. 77, pp. 16–35, 1916.

[41] J. S. Marshall and W. M. Palmer, "The distribution of raindrop with size," *J. Meteorol.*, vol. 5, pp. 165–166, 1948.

[42] M. Abramowitz and I. A. Stegun, Eds., *Handbook of Mathematical Functions with Formulas, Graphs, and Mathematical tables*, 9th ed, New York: Dover, 1972.

[43] H. Liebe, "An atmospheric millimeter-wave propagation model," *Int. J. Infrared Millimeter-Wave*, vol. 10, pp. 367–378, 1989.

[44] H. Czekala and C. Simmer, "Microwave radiative transfer with nonspherical precipitating hydrometeors," *J. Quant. Spectr. Radiat. Transf.*, vol. 60, pp. 365–374, 1998.

Frank Silvio Marzano (S'89–M'99–SM'03) received the Laurea degree (*cum laude*) in electrical engineering and the Ph.D. degree in applied electromagnetics from the University "La Sapienza" of Rome, Italy, in 1988 and 1993, respectively.

In 1993, he collaborated with the Institute of Atmospheric Physics, CNR, Rome, Italy. From 1994 to 1996, he was with the Italian Space Agency, Rome, Italy, as a Postdoctoral Researcher. After being a Lecturer at the University of Perugia, Italy, in 1997 he joined the Department of Electrical Engineering and the Center of Excellence CETEMPS, University of L'Aquila, Italy, coordinating the Satellite and Radar Remote Sensing Laboratory. In 2005 he joined the Department of Electronic Engineering, University "La Sapienza" of Rome, where he presently teaches courses on antennas, propagation and remote sensing. His current research concerns passive and active remote sensing of the atmosphere from ground-based, airborne, and spaceborne platforms and radio propagation topics in relation to incoherent wave modeling, scintillation prediction and rain fading analysis along satellite microwave links.

Dr. Marzano received the Young Scientist Award of the XXIV General Assembly of URSI in 1993. In 1998, he was the recipient of the Alan Berman Publication Award (ARPAD) from NRL, Washington, DC. Since January 2004, he has been acting as an Associate Editor of *IEEE Geoscience Remote Sensing Letters*.